


Article

Effects of Ultrasonic Impact Treatment on the Stress-Controlled Fatigue Performance of Additively Manufactured DMLS Ti-6Al-4V Alloy

Peter Walker ¹, Sinah Malz ², Eric Trudel ¹, Shaza Nosir ¹, Mostafa S.A. ElSayed ^{1,*} and Leo Kok ³

¹ Department of Mechanical and Aerospace Engineering, Carleton University, Ottawa, ON K1S 5B6, Canada; PeterMWalker@cmail.carleton.ca (P.W.); EricTrudel@cmail.carleton.ca (E.T); ShazaNosir@cmail.carleton.ca (S.N.)

² Department of Mechanical Engineering, University of Rostock, 18051 Rostock, Germany; sinah.malz@uni-rostock.de

³ Department of Advanced Structures, Bombardier Aerospace, Toronto, ON M3K 1Y5, Canada; leo.kok@aero.bombardier.com

* Correspondence: mostafa.elsayed@carleton.ca; Tel.: +1-613-520-2600 (ext. 4138)

Received: 10 September 2019; Accepted: 18 October 2019; Published: 8 November 2019



Abstract: Additive manufacturing (AM) offers many advantages for the mechanical design of metal components. However, the benefits of AM are offset to a certain extent by the poor surface finish and high residual stresses resulting from the printing process, which consequently compromise the mechanical properties of the parts, particularly their fatigue performance. Ultrasonic impact treatment (UIT) is a surface modification process which is often used to increase the fatigue life of welds in ship hulls and steel bridges. This paper studies the effect of UIT on the fatigue life of Ti-6Al-4V manufactured by Direct Metal Laser Sintering (DMLS). The surface properties before and after the UIT are characterized by surface porosity, roughness, hardness and residual stresses. Results show that UIT enhances the fatigue life of DMLS Ti-6Al-4V parts by suppressing the surface defects originating from the DMLS process and inducing compressive residual stresses at the surface. At the adopted UIT application parameters, the treatment improved the fatigue performance by 200%, significantly decreased surface porosity, reduced the surface roughness by 69%, and imposed a compressive hydrostatic stress of 1644 MPa at the surface.

Keywords: fatigue life improvement; materials characterization; additive manufacturing; ultrasonic impact treatment; DMLS

1. Introduction

Additive Manufacturing (AM) offers great promise to the medical [1], aerospace [2], automotive and defense fields [3–5]. It provides the advantage of building complex geometries by fabricating 3D objects one layer at a time using rendered CAD models [6], as a result, several techniques of AM have been developed, including, Electron Beam Melting (EBM) [7], Selective Laser Sintering (SLS) [8], Selective Laser Melting (SLM) [9], and Direct Metal Laser Sintering (DMLS) [10]. Another advantage of AM lies within the wide range of materials that can be manufactured such as plastics [11], metals [3,12–14], ceramics [15], concrete [16] and fiber reinforced polymers [17], among others. The AM of metals are of particular interest to the production of dental implants, aerospace components, and automotive structures [18]. Today, stainless steel [19,20], nickel alloys [21,22], aluminum alloys [23,24] and titanium alloys [25,26] are common materials for metals AM.

DMLS is one of the most common AM processes for 3D printed metals because it maintains dimensional control while producing complex features at high resolution [3]. There are two primary methods of manufacturing by DMLS: powder bed and powder deposition [27]. Powder bed methods rely on a high energy source, typically a laser (although some similar systems use electron beams), to locally sinter or melt metal particles on a powder platform. New powder layers are periodically added while the platform is levelled to accommodate the addition of new material. The 3D model is constructed in a single vertical direction [6]. Alternatively, powder deposition directly deposits the metal powder and melts it in place using a high-powered laser [28]. Unlike the powder bed method, which is typically restricted to one type of alloy, powder deposition has the ability to include different metal powders for functionally graded materials [29].

This process however, also has a number of drawbacks. Parts produced via DMLS typically have poorer mechanical properties compared to those produced by traditional means, which has relegated the potential uses to prototypes and short-term tooling operations [30]. Incomplete powder melting often leads to very rough surface finish and porosity, which in addition to being aesthetically displeasing also compromises fatigue life and can be a significant issue for wetted surfaces of air and water craft [29,31]. In addition, the rapid heating and effective quenching of the metal results in a highly martensitic microstructure in most alloys [32]. While this produces a material with a high yield strength, it is also intensely brittle [32]. Though the microstructure resists the formation of cracks, once the cracks themselves form, the propagation of the cracks is quite rapid [33]. The high temperature gradient involved in these processes frequently causes thermal stress that compromise the fatigue performance of metals produced by DMLS techniques.

Titanium alloys such as Ti-6Al-4V are commercially available for additive manufacturing. Due to its high strength to weight ratio and fracture toughness, it is an ideal alloy for a wide range of applications in the aerospace and biomedical engineering fields [34]. For instance, Ti-6Al-4V alloy is used in dental laboratories for medical implants and prosthetics due to its corrosion resistance, high specific strength as well as its biocompatibility characteristics. AM also allows for the creation of porous titanium structures that help facilitating bone ingrowth and adhesion for implants [35]. Advances in topology optimization allows for hyper-efficient geometries to be produced exclusively through additive manufacturing. One notable example includes the Airbus A320 nacelle hinge bracket which was eventually produced by AM [36]. With the many advancements in the field of AM, the production of titanium parts has become economically viable. Hence it is imperative that the fatigue properties are improved for the next generation of additively manufactured titanium components [33,37–40]. In the case of Ti-6Al-4V, the hexagonal close-packed (HCP) α phase and trace amounts of a body centered cubic (BCC) β phase are almost entirely replaced with the martensitic α' phase. The poor surface finish and high porosity are also factors that offset the microstructural characteristics on the fatigue performance.

The demand for functional AM parts has been rising as high reduction in assembly costs are available coupled with decreases in mass. One example is the fuel nozzles for the General Electric (GE) LEAP engine have been additively manufactured to be 25% lighter while eliminating previous models that required laborious assembly. Its successful design has now been 3D printed more than 30,000 times since its conception [41]. With the increasing demand for metal AM, researchers have begun to develop techniques to improve the fatigue performance by improving the surface finish and by inducing compressive residual stresses at the surface. Shot peening [42], Ultrasonic Nanocrystal Surface Modification (UNSM) [43–46] and grit blasting [47] are well known examples of beneficial treatments on AM of metals. However, none of these processes were able to address all the following simultaneously: surface roughness, surface porosity, fatigue life and tensile residual stresses.

Studies have shown that Ultrasonic Impact Treatment (UIT) improves the surface finish and fatigue properties in the field of post-welding [48]. UIT is a process in which an indenter vibrating at ultrasonic frequencies slides over a surface. This treatment plastically deforms the surface, improving the surface finish while inducing and redistributing residual stress in the part resulting in enhanced

fatigue life [48]. UIT devices operate by inducing plastic deformation from the indenter or impact needle by first exciting a transducer by a controlled voltage input. The power source directly controls the oscillations exhibited by the transducer, which sends its frequencies to the sonotrode (ultrasonic horn) [48]. The research of E. Statnikov et al. [49] compared a variety of methods that improve the fatigue life of welded joints. Other similar methods include Hammer Peening, Shot Peening and Tungsten Inert Gas (TIG) dressing. An improvement of 65% was observed in the UIT joints. In B.N. Mordyuk et al. [50] investigated the enhancements that occur in the surface layer of ultrasonic impacted specimens. It was concluded that the compressive residual stresses and work hardening of the surface layer attributed to the improvement in fatigue properties of processed specimens. A.I. Dekhtyar et al. [51] concluded that at high stress levels, UIT-processed Ti-6Al-4V has a fatigue life that is twice of the pristine (untreated) samples, and a roughness reduction R_a of 75%. While UIT is widely used in fatigue improvement of welded joints, the aim of this paper is to treat the surface of Ti-6Al-4V specimens produced by DMLS using UIT to improve roughness, increase hardness and induce surface compressive residual stresses to enhance the fatigue life of the components.

It is well known that the resistance to tensile fatigue of a metal will increase by the addition of compressive stress [37]. UIT compares favorably to other surface treatments due to its higher impact forces [48]. Quantifying this level of stress by the cold working of the surface for titanium alloys can prove to be beneficial in future engineering applications, as evaluation of impact forces between the pins and the metal surface of UIT is under researched. Force estimations for other cold hardening treatments such as shot peening have been measured. One method used acoustic emissions for velocities of 30 to 88 m/s; however, this was not able to properly determine the impact force [52]. Many other techniques have been developed for measuring shot peening impact forces, which include a shot peening intensity detector; however, most methods cannot be directly applied to measure forces for an ultrasonic impact device [53]. Research into the optimization of UIT parameters has led to the use of oscilloscopes for defining the impact characteristics between the pin and the metal surface [48,54]. The frequencies were able to illustrate the ultrasonic deformations and elastic recovery of the process. The frequency patterns are also able to show the stochastic nature of the impacts that are influenced by both the impact depth and plastic deformation. An additional experiment presented in this paper is conducted to quantify impact forces during UIT on DMLS printed titanium specimens.

2. Materials and Methods

2.1. Specimens Manufacturing

Flat dog-bone fatigue specimens were manufactured in accordance to ASTM E466-15 [55] for force controlled fatigue testing. Figure 1a illustrates the dimensions of the dog-bone in millimeters. The titanium dog-bone specimens were built using Ti-6Al-4V grades 23 powder from AP&C, composed of between 5.5 and 6.75 wt% aluminum, 3.5 and 4.5 wt% vanadium and <0.25 wt% iron and trace amounts of <1 wt% impurities such as oxygen, nitrogen and hydrogen with the balance being titanium [56]. The 3D printer used to manufacture the specimens was an EOSINT M290/400W machine following a general process parameter of layer thickness of 30 μm and volume rate of 5 mm^3/s where the volume rate is a measure of the build speed during laser exposure of the skin area [57]. The process parameters are optimized in such a way as to provide mechanical properties comparable to other literature [58]. The particle size ranged from 15 to 23 μm and the printing layers thickness were 60 μm . The specimens were heat treated in accordance to AMS 2801 to relieve the residual stress induced by the rapid melting and solidification that takes place during the printing process [26,59]. Figure 1b shows the printing orientation, where the printing platform lies in the x-y plane. A single 2D layer is formed on the platform when the laser beam sinters particles starting from the left end and moving towards the right end of the dog-bone shown in Figure 1.

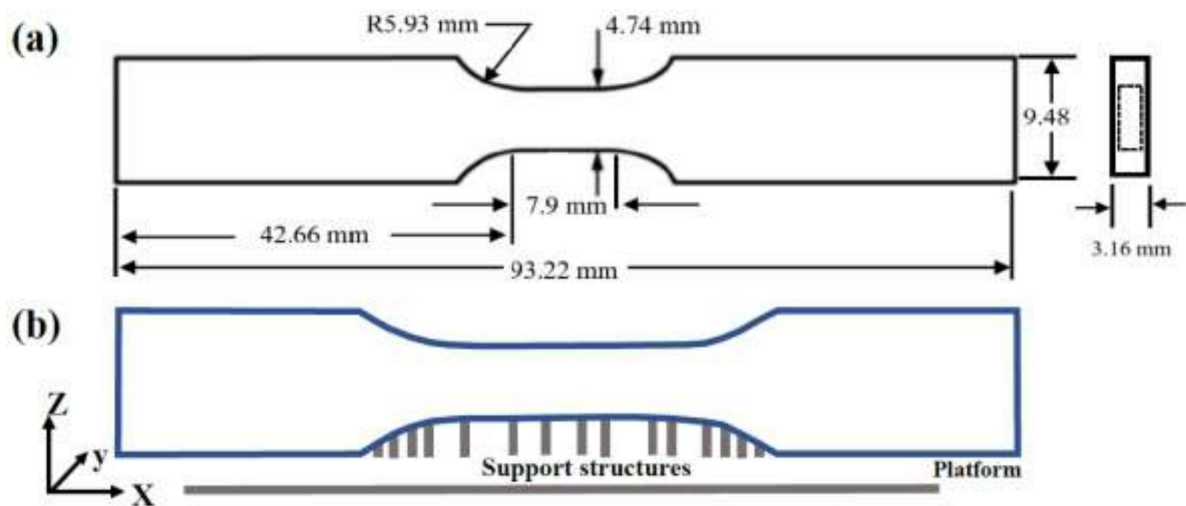


Figure 1. Specimens design and preparation. (a) Schematic of flat sheet fatigue specimen with rectangular cross-section; (b) orientation of the specimens during DMLS manufacturing process.

When the layer is completed, the platform is levelled in the z-axis allowing a new layer to be added on top of the previous one. Wire Electrical Discharge Machining (EDM) is a precise cutting technique that minimizes the need for excessive post processing machining and was used to breakaway support and remove the specimens from the platform [60]. Lastly, the edges were then polished using an emery cloth of grades 120 and 220 [61].

2.2. UIT Device

The UIT device, displayed in Figure 2, is a 20k Ultrasonic Impact Treatment device, DW-CJ20-1000 produced by Dowell Ultrasonics [62], typically used as a hand-held tool for post-welding processing. It consists of a power supply, shown in Figure 2a, the UIT tool, shown in Figure 2b, the impactor head, shown in Figure 2c and the ultrasonic generator, shown in Figure 2d. It is equipped with slots for four impactors, but for the purposes of this experiment—only one impactor was used, as illustrated in Figure 2c. To provide automated control, a custom-built fixture is used to attach the device to the spindle of a Computer Numerical Control (CNC) Mill. Figure 2e shows the treatment path programmed to minimize the surface roughness while obtaining a uniformly deformed surface. The scanning speed of the CNC machine was set to 1000 mm/min. The spacing between the scans is known as an interval. Amplitude control of the device is controlled by a Fagor 8035M controller [63]. A constant amplitude of 57% of 40 μm was used during treatment as testing showed that this amplitude provided the most consistent plastic deformation of the surface without damaging the samples. The interval for treating titanium alloys typically ranges between 10 and 70 μm [43–46,64]. The path contours were chosen to increase outwards at 71.1 μm intervals to match previous efforts and research into surface treatments on titanium [43,44,65].

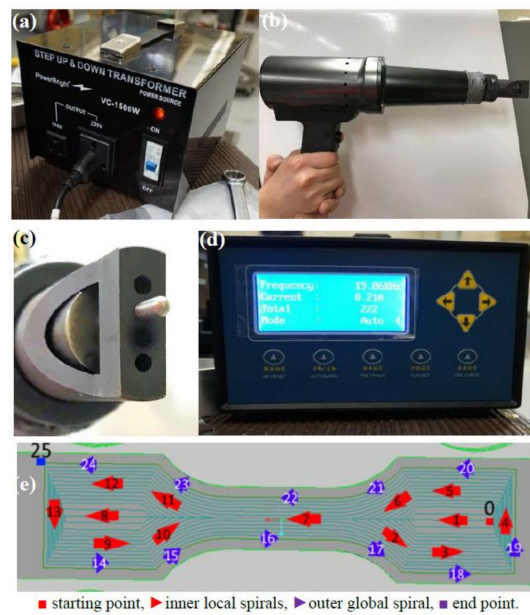


Figure 2. UIT system and application pattern. (a) Power supply unit; (b) side view of the UIT device; (c) front view of the UIT device showing impactor position; (d) ultrasonic generator; (e) schematic of treatment path.

2.3. Specimens Fixture

To apply the UIT a new fixture was designed, as shown in Figure 3. The Ti-6Al-4V specimens were clamped to an aluminum plate that was supported by four steel rods and four aluminum sleeves, as illustrated in Figure 3. The plate can freely slide along the rods and its motion range is limited to four high precision springs from McMaster Carr [66] placed between the plate and the end of the supporting rods. Compressing the springs allows for a constant static force to be applied onto the samples during treatment. By pushing the UIT device into the plate and compressing the springs a certain distance, the amount of static force can be determined. Aluminum cutting fluid [67] was used to lubricate the rods so that the plate could freely move by the springs. For this experiment, a static force of 30 N was applied at the tool specific constant frequency of 19.86 kHz.

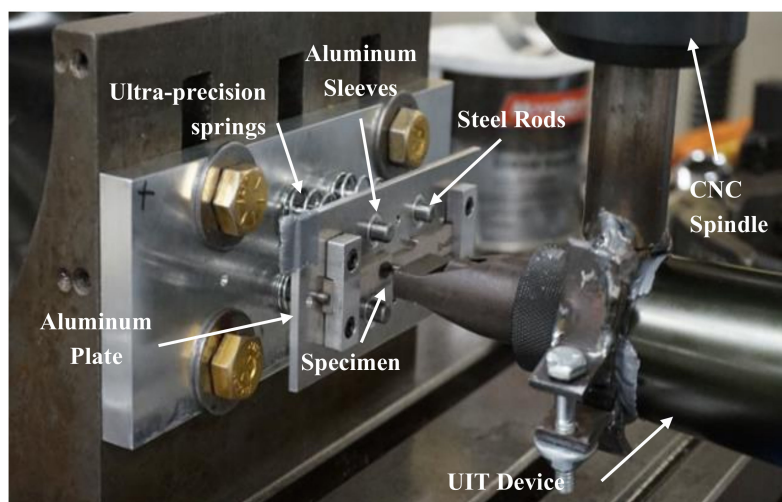


Figure 3. Spring assembly fixture with a clamp mounted to the CNC machine.

2.4. Fatigue Testing

Force controlled fatigue tests were undertaken with a servo-hydraulic 810 Material Testing System (maximum load 100 kN) [68]. The MTS consists of an upper and a lower clamping grip. For consistent and precise alignment, a fence was attached to each grip. All specimens were tested under a clamping pressure of 5.52 MPa, frequency of 25 Hz, maximum stress level of 400 MPa and mean stress level of 200 MPa.

2.5. Microscopy

Microscopic observations were conducted using a combination of optical and scanning electronic microscopy. The former was performed with an Inverted Trinocular Metallurgical Microscope including an AmScope 18 MP MU 1803 Camera [69]. Electron microscopy was performed with a Zeiss GeminiSEM 500 at the University of Ottawa's Centre for Photonics Research [70].

2.6. Roughness

Roughness measurements were performed using DektakXT Stylus Profiler by Bruker [71]. A Peak and Valley analysis was conducted to determine the relative roughness of each sample. As illustrated in Figure 4, a lateral and a longitudinal line scan is performed on each side of a specimen. The scans intersect to form a cross. Roughness measurements were taken over 2 mm in each direction and the results are averaged.

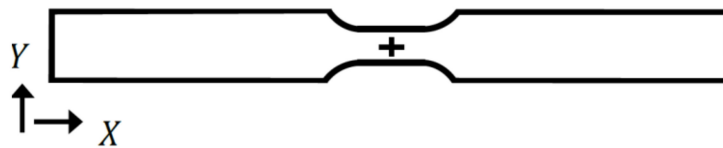


Figure 4. Orientation of line scans for surface roughness.

2.7. Hardness

Rockwell hardness was used to analyze the difference in hardness between treated and untreated specimens following the testing standards of ASTM E18-18a [72]. A Rockwell C test was performed using a test force of 150 kgf on treated and untreated specimens using “The Portable Rockwell Hardness Tester” by Bowers [73].

2.8. Residual Stresses by X-ray Diffraction

Residual stress is defined as the stress remaining in a solid material after an applied force or plastic deformation has taken place. UIT imposes a high plastic strain at the surface of the treated surface, which results in compressive residual stresses. X-ray diffraction (XRD) is a non-destructive method for analyzing the residual stress in a material and is the method of choice for this paper.

Chemical etching of the surface was applied to remove suspected amorphous or oxide material layers, potentially caused by initial stress relaxation treatment. The effect of etching the surface and XRD quality of the scans is illustrated in Figure 5. Peak shapes become much clearer and better defined. It is also important to note that mechanical polishing or grinding will cause lattice strains to be formed at the surface and are not recommended for cleaning samples for residual stress measurements [74]. To conserve and reveal the surface stress layer, a chemical etchant—Kroll's Reagent—was used to remove small amounts of material from the top of the treated and untreated titanium specimens [75,76]. The amount of material removed from the surface was measured to be on average $\sim 8 \mu\text{m}$.

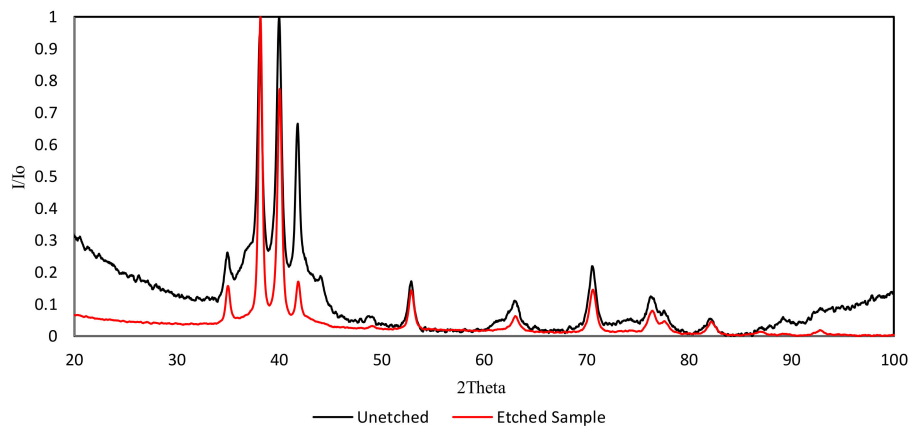


Figure 5. XRD Comparison between etching and without etching.

It is suggested by P. Mercelis et al. [40] that the surface porosity of DMLS manufactured parts poses difficulties for measuring residual stresses due to the presence of zero-stress porosity borders. Stress discontinuities on the surface result in lower residual stresses to be measured than in reality. Hence, cleaning the surface of the samples through etching would also help to reduce the effects of roughness and porosity that may negatively affect the XRD measurements.

The XRD measurements were taken using a Malvern Panalytical Emperyeen [77], shown in Figure 6b. The machines power was set to 40 kV with a current of 40 mA for a strong signal response—particularly at higher rocking angles. A half degree diffraction slit was used with a mask size of 2 mm and an anti-scatter slit of 2°. The diffraction arm was a Branson Bragg attachment with a 0.04 mm slit. The incident arm was equipped with a 0.04 mm slit and a 9.1 mm opening.

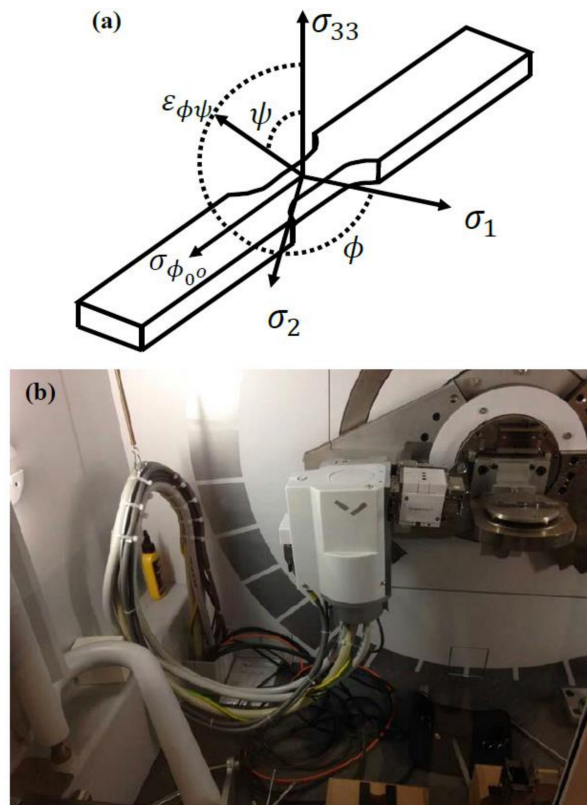


Figure 6. XRD System. (a) Drawing of diffraction directions along the surface and at angles ϕ and ψ . Both σ_1 and σ_2 are perpendicular and reside in the plane of the specimen surface; (b) sample oriented at 0° on multi-purpose stage of Emperyeen system.

The analysis method for computing the stress tensor was the Winholtz-Cohen Least squares Analysis [78]. A total of 36 measurements per sample were used for the analysis, each representing a unique tilt and azimuth angles. The chosen x-ray elastic constants of the DMLS Ti-6Al-4V specimens where $2.355 \times 10^{-5} \text{ MPa}^{-1}$ as the S_2 constant and $-2.9877 \times 10^{-6} \text{ MPa}^{-1}$ for the S_1 constant [65,79]. These constants are the interplanar properties for the bulk alpha phase of the metal alloy. The X-ray wavelength was set to 1.519 \AA .

The specimen coordinate system had the azimuth or phi (ϕ) of value zero lined up with the horizontal direction (X) as illustrated by the cross seen in Figure 6a. The tilt angles or psi (ψ) is shown in Figure 6a where the 0° begins at 90° from the samples surface.

2.9. Estimation of Impact Force

A piezoelectric force sensor was used to estimate the impact forces at the surface during treatments. To measure the reaction forces at the surface; an alternative fixture was developed to house the sensor and impact plates. This fixture contains linear ball bearings instead of steel bushings to guide the plate, as seen in Figure 7a. The support rods were thickened, and the four previous compression springs were replaced with two larger springs. Proper calibration using a strain gauge was performed so that the correct amount of static force could be determined based on the compression of the spring system. The sensor was attached to the moving plate on the fixture with a titanium specimen used as an impact cap. Operation of the UIT during the estimation of impact force was controlled in much of the same way as during the UIT. The sensor would register the forces from the UIT impacts on the titanium cap. For simplistic design, the cap was a repurposed fatigue specimen.

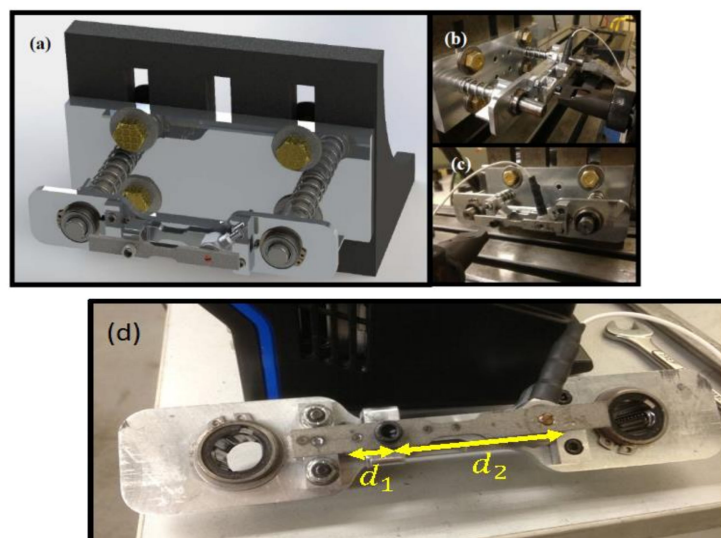


Figure 7. Experimental setup for impact force estimation. (a–c) Impact force fixture; (d) impact areas and distances.

Due to the design of a repurposed fatigue specimen as an impact surface, reaction forces can be registered by the sensor depending on its distance from the impact. The titanium cap was treated as a double supported beam with one end constrained by a bolt and the other end constrained by the sensor using a double-sided thread. The double supported beam assumption allows for a simple ratio to be developed based equilibrium of moments to solve for the actual impact forces. A diagram of the impact set up can be seen in Figure 7b,c The selected distances between the sensor and the impact region are displayed in Figure 7d, where d_1 is 8.89 mm and d_2 is 47.752 mm. The relationship between the sensor reaction force and the impact force is presented in Equation (1).

$$F_{\text{impact}} = -F_{\text{Sensor}} \cdot \frac{d_2}{d_1}, \quad (1)$$

where F_{impact} is the force of impact and F_{sensor} is the force registered by the sensor.

Data acquisition was performed using a Lecroy WaveSurfer 3000 Oscilloscope [80]. The force sensor was a PCB piezoelectric force sensor model 208C05. The force range of the sensor was 0 to 4500 kgf. The conversion from voltage to force was assumed to be linear with a sensitivity of 0.2170 mV/N ($\pm 15\%$).

Calibration of the sensor was checked using test procedure AT501-5. The amplifier gain of the sensor was set to 100. Additional shrink tubing was added between the sensor and the wire nuts to prevent vibrations during testing from unscrewing and ejecting the wires from the sensor. The peak voltage read by the sensor for a short ultrasonic impulse was regarded as the impact force for a given static load. The compression of the springs drives the static load with the total stiffness of the system equal to 3.06 N/mm.

2.10. Microstructural Analysis

The effect of the UIT on the microstructure of the material was investigated through Light Optical Microscopy (LOM) and Scanning Electron Microscopy (SEM), the latter being done with both secondary electron and backscatter electron (BSE) detection. Metallographic samples were cut from tensile specimens and mounted in a resin made from phenocure combined with $\sim 15\%$ Technotherm conductive powder for improved SEM performance [81]. Samples were polished with an Allied High Tech MetPrep 3 system with a PH-3 powerhead [82], using SiC paper with a CAMI Grit designation ranging from 120 to 1200 [82], followed by a polish with a suspension of 30% 0.3 μm alumina particles and a final polish of 30% H_2O_2 and 30% 0.05 μm particles [83]. Samples were etched prior to microscopy, using both classical Kroll's reagent and a 10% HF etchant for better grain boundary definition, in keeping with ASTM Standard E407-99 [84].

3. Results and Discussion

3.1. Fatigue Life

A stress-controlled fatigue test was conducted according to DIN 50100 [85] and based on a logarithmic normal distribution. Table 1 displays the fatigue life of Ti-6Al-4V specimens before and after UIT application. The specimens were tested in a servo-hydraulic 810 Material Test system (MTS) at a peak stress level of 400 MPa and minimum stress of 0 MPa. The average number of cycles for the treated and untreated specimens is compared in Figure 8.

Table 1. Fatigue life of treated and untreated specimens at 400 MPa.

Specimen Number	1	2	3	Average
Untreated	2.39×10^4	2.77×10^4	4.02×10^4	2.90×10^4
Treated	8.47×10^4	8.84×10^4	9.63×10^4	8.97×10^4

Evaluation of the fatigue performance of DMLS Ti-6Al-4V shows that the fatigue life of untreated specimens is 77% lower than handbook values [37]. The results in Table 1 and Figure 8 show that the fatigue life of treated specimens at 400 MPa corresponds to a 200% increase compared with that of untreated specimens. In other words, the lifetime of the treated samples is three times as long as untreated samples. D. Cattoni et al. [47] only achieved a 4% fatigue improvement by blasting Ti-6Al-7Nb, whereas A.I. Dekhtyar et al. [51] prolonged the lifetime of Ti-6Al-4V, manufactured using the cost-effective blended elemental powder metallurgy technique, by two orders of magnitude after applying ultrasonic impact treatment.

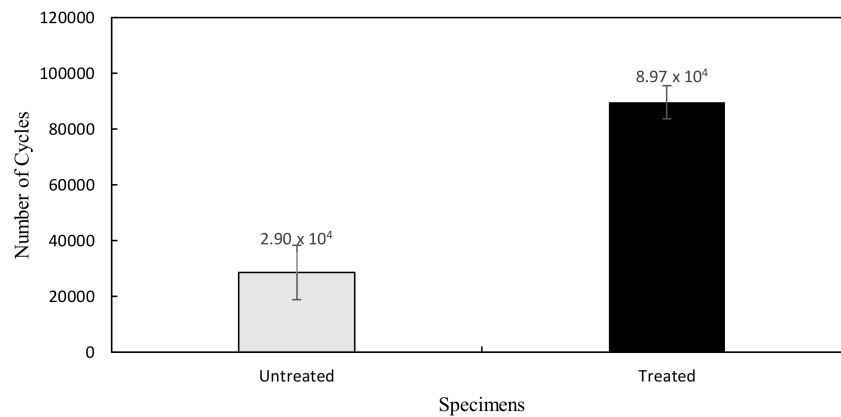


Figure 8. Average fatigue life of treated and untreated Ti-6Al-4V specimens tested at 400 MPa.

3.2. Surface Microscopy

Figure 9a illustrates the surface of Ti-6Al-4V as manufactured by DMLS, which is dominated by the partial melted powder spheres from the additive manufacturing process along with numerous hills and valleys. Despite extensive cleaning in an ultrasonic bath with organic solvents, the rough surface still traps surface contaminants. Tracklines formed by the solidification of the powder bed layers are also visible. These further add to the roughness of the surface and can become sights of crack nucleation and potentially propagation as well [59]. Figure 9b shows the boundary zone between the treated and untreated zones, and the contrast is quite striking. The treated zone is of relatively uniform height, with the spherical powders having been plastically deformed by the impact treatment. However, even this small image of the boundary zone shows that the boundary is quite ragged, with “peninsulas” jutting out from the treated zone and small “islands” of treated area that are separated from the treated zone. The fully treated zone is shown in Figure 9c, and from simple observation it is clear that the surface is much less rough and thus much less conducive to crack nucleation.

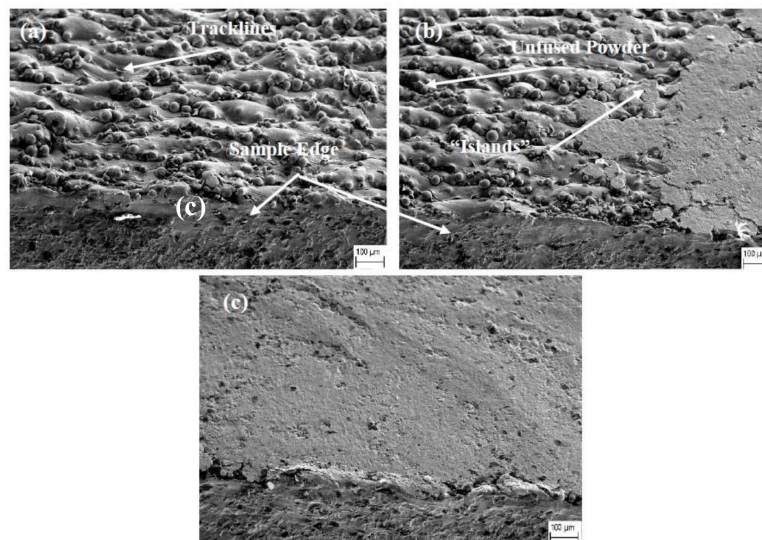


Figure 9. Specimens surface microscopy. (a) Surface of untreated specimen; (b) boundary zone between treated and untreated zone; (c) treated surface of specimen. All images taken with SE2 detector at 15 kV.

The UIT had successfully improved the surface finish of the DMLS Ti-6Al-4V, which corresponds to the improved fatigue performance. Unlike the surface of metals treated by grit blasting and UNSM, the surface of UIT specimens is not jagged. This is due to the combination of vibrating the indenter at ultrasonic speeds while sliding across the surface.

3.3. Roughness

The results from the DektakXT profilometer used to perform a Hills and Valleys profile on both treated and untreated specimens is displayed in Figure 10. The untreated surface is 3.2 times rougher than the treated surface. A control factor for fatigue strength in specimens with high surface roughness is crack propagation, whereas for specimens with low surface roughness it is crack initiation [86]. Additional stress raisers are introduced as a result of rougher surfaces; increasing the number of potential crack initiation sites. Stress raisers as a result of rougher surfaces will reduce crack initiation life and the fatigue limit. Therefore, smooth surfaces can be considered as a contributing factor to the improved fatigue life, as seen by the fatigue performance of the treated samples with improved surface roughness.

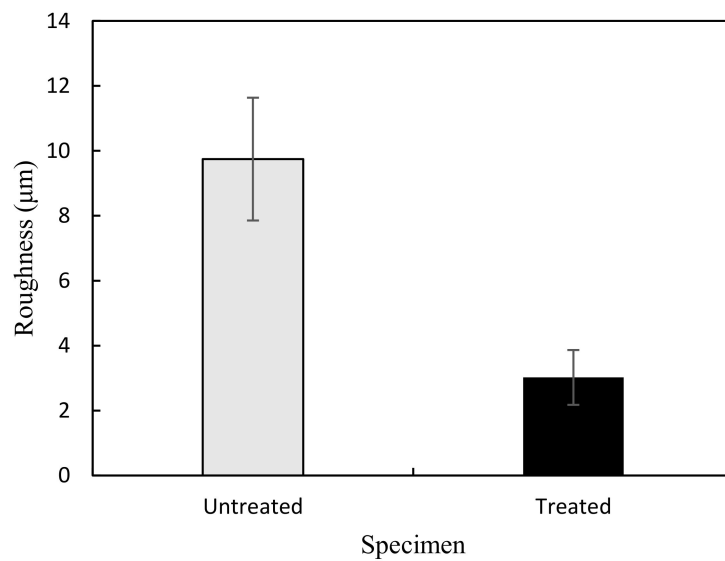


Figure 10. The average roughness of treated and untreated specimens measured by DektakXT.

The effects of UIT on the AM titanium surface are also observed using a two-dimensional map scan as shown in Figure 11. The peaks and valley analysis clearly illustrate the effects on both surface roughness and surface porosity. The untreated surface has a much higher density of hills and valleys unlike the treated surface, which has a much more uniform surface and less pronounced differences between peaks and valleys. The highly irregular surface of the DMLS titanium is attributed to the manufacturing process and incomplete fusion. The final layer of metal powder during printing is not completely melted and produces a very rough surface. The high impact forces of the UIT helps diminish these effects and improves the surface quality and fatigue performance.

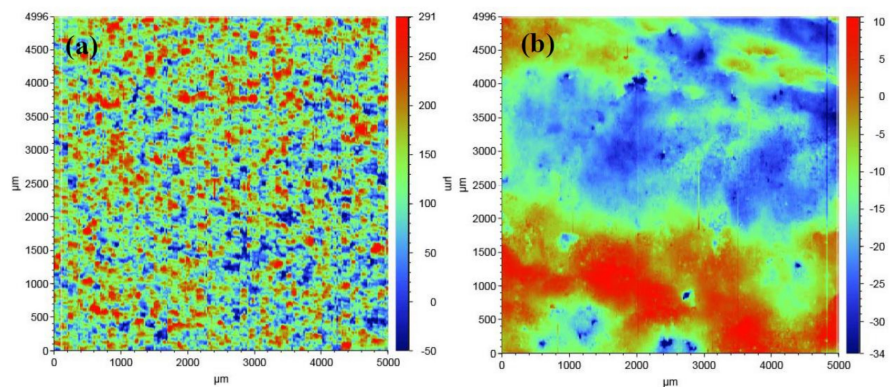


Figure 11. Roughness map scans between the (a) untreated and (b) treated surfaces.

3.4. Hardness

The results from Rockwell C tests performed using a test force of 150 kgf are illustrated in Figure 12, the treated specimens are on average 21% harder than the untreated specimens. However, it is important to note that the hardness is highly variable in both samples. The lowest hardness values from the treated sample are roughly equivalent to the hardest values from the untreated sample. This variability is likely due to the very rough surfaces of both samples. As a result, no statistical conclusion can be drawn from the hardness data about which sample is harder overall. It can be said that the hardness of the treated specimen is more consistent than that of the untreated specimen, and that there are points on the treated specimen that are harder than points on the untreated specimens. This possible increase in hardness at certain points could be attributed to the work hardening done by the UIT, a result of the increase in dislocations density at the surface which will resist further deformation. The increase in hardening could lead to a resistance to crack initiation sites in those locations, which corresponds to an increase in fatigue life [65].

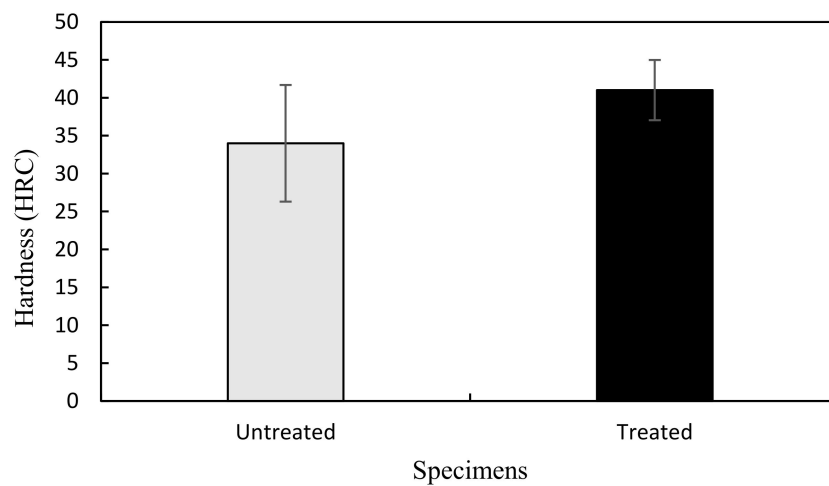


Figure 12. The average hardness of treated and untreated specimens from the Rockwell C test.

3.5. Residual Stresses

For values ranging between 2.5 and 5 μm in depth, residual stresses play a predominant role in improving fatigue life [51]. Based on the results of the residual stress and residual strain measurements, shown in Tables 2 and 3, respectively, the success of the UIT can be attributed to high compressive stresses at the surface of the specimens.

Table 2. Residual stress results (MPa).

Component	Treated—Plane 114		Untreated—Plane 211	
	Stress (MPa)	Error (MPa)	Stress (MPa)	Error (MPa)
σ_{11}	-1.9×10^3	45	-3.0×10^2	20
σ_{22}	-1.8×10^3	45	-2.8×10^2	22
σ_{33}	-1.2×10^3	26	-2.1×10^2	12
σ_{12}	27	6.0	-0.9	2.7
σ_{13}	-1.1	6.0	1.1	2.5
σ_{23}	37	22	19	9.3
σ_{VM}	6.0×10^2	48	84	21
$I_1/3$	-1.6×10^3	68	-2.7×10^2	32

Table 3. Residual strains results.

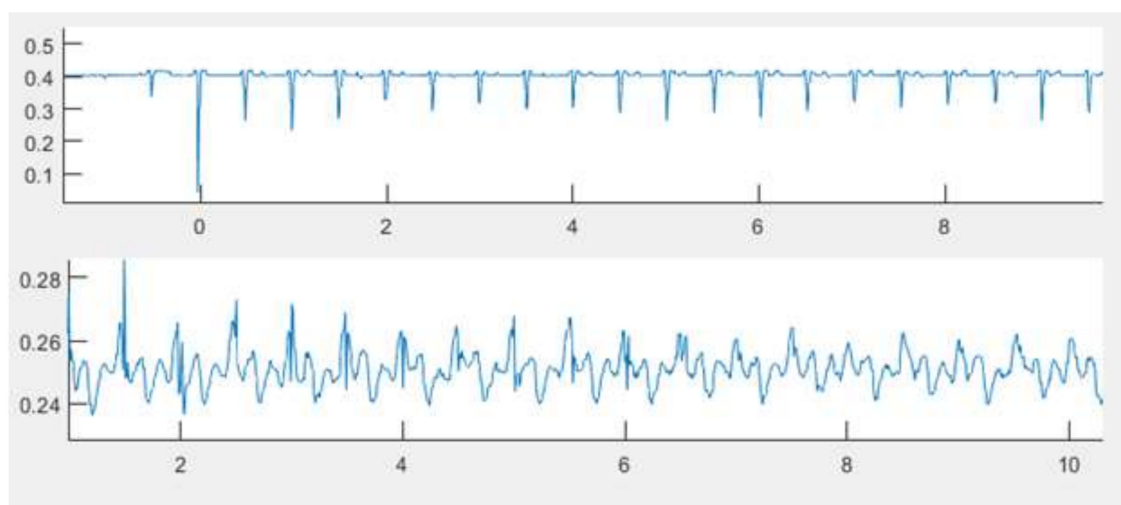
Component	Treated—Plane 114		Untreated—Plane 211	
	Strain	Error	Strain	Error
ϵ_{11}	-7.2×10^{-3}	1.8×10^{-4}	-1.1×10^{-3}	7.9×10^{-5}
ϵ_{22}	-6.7×10^{-3}	1.7×10^{-4}	-9.7×10^{-4}	7.8×10^{-5}
ϵ_{33}	2.1×10^{-6}	-4.5×10^{-8}	-1.5×10^{-4}	8.8×10^{-6}
ϵ_{12}	3.2×10^{-4}	7.4×10^{-5}	-1.0×10^{-5}	3.4×10^{-5}
ϵ_{13}	-1.3×10^{-5}	7.4×10^{-5}	1.2×10^{-5}	3.1×10^{-5}
ϵ_{23}	4.4×10^{-4}	2.7×10^{-4}	2.2×10^{-4}	1.2×10^{-4}
ϵ_{VM}	4.7×10^{-3}	5.6×10^{-4}	6.6×10^{-4}	2.4×10^{-4}

These stresses help minimize the generation of tensile stresses at the surface due to cyclic loadings thereby suppressing crack formation and nucleation [49].

The high compressive stresses help minimize the damage caused during cyclic loading by shifting the mean stress downwards. This eventually leads to longer life in the part as compressive stresses will lower the stress ratio. Experimental data has shown that as the stress ratio becomes increasingly negative, longer lives were measured. This can be explained by compressive surface stresses preventing dislocations from moving within the material. The hydrostatic stresses for each tensor reveal the same trend; the untreated sample had a hydrostatic stress of -265 MPa while the treated sample had -1644 MPa. A high compressive hydrostatic stress could also represent an increase in fatigue resistance due to UIT.

3.6. Impact Force Quantification

The impact force with respect to the variation of compressive static force was obtained. The results show that for a static force between 0 and 10 N, the impact force is relatively constant and is on average 20 kN. After which, the force steadily increases up to 72 kN when the static force is equal to 30 N. The trend is slightly parabolic and impact forces at zero newton of static force were measured to be slightly higher than at 10 N of static force. The impact force on the fatigue samples is thus 72 ± 11 kN. For every second, approximately $2.1 \times 10^4 \pm 6.0 \times 10^2$ impacts occur at a static force of near zero, seen in Figure 13. This would mean that for an amplitude of 57% of 40 μm the average absolute vertical speed of the indenter is 0.94×0.03 m/s.

**Figure 13.** Force vs. time as measured by the force sensor.

The high impact forces are due to metal on metal deformation between the steel pin indenter and the titanium surface. High forces are registered due to the high modulus of elasticity of the mediums

and by the ultrasonic vibrations and stress waves [48]. Another factor to consider for high impact forces are due to impulses occurring over a very short time period. The force versus time plots in Figure 13 show the readings of the oscilloscope of a low static force. When minimal static forces are present, the force pattern is rather predictable and consistent. As the static force is increased, the level of stochastic behavior increases dramatically, as seen in Figure 14. The increased randomness is attributed to the increase in plastic deformation which creates widening gaps with varying depth. The subsequent plastic deformation on the surface will then begin to slightly alter the impact forces slightly due to both work-hardening and rebounding forces from the support springs.

Impact Force (kN) vs. Static Load (N)

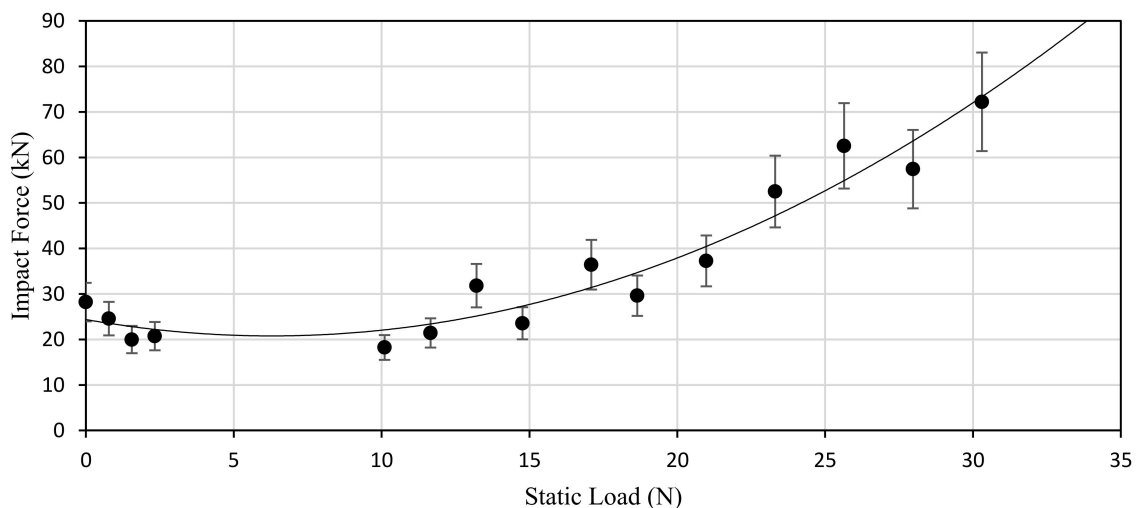


Figure 14. Impact force (kN) vs. static load (N).

The impact force on the surface, given one UIT needle, can be replicated if an equivalent force is used to generate the plastic deformation. Hence, other work hardening processes can achieve the same effects of the UIT if similar impact forces are used combined with a transverse velocity along the surface. Possible errors in the impact force assessment can be attributed to off-axis impact forces. Loads applied to the side of the sensor may cause higher than normal readings. This is a result of coupling forces acting on the sensor. However, calibration between the distances of the applied load to sensor was made to ensure that off-axis effects are diminished.

The saturation point of the sensor was reached once the static forces approached 30 N as it was close to the maximum range of the sensor. Any other force impact reading after the saturation point would not have been reliable as the sensor would have been destroyed. It is unknown what impact forces are possible after 30 N as extrapolation of the data is within an area of high uncertainty. The results are also calibrated for the UIT fixtures set up which includes a spring-loaded system. The springs vibrations combined with the indenter's oscillations creates a varied and stochastic process leading to large error bounds during the treatment process. The reaction forces of the springs may also contribute to higher than normal impact forces. Due to the calibration of the sensor in combination with the fixture, there is a level of specificity in the force calibration curve that may limit its applicability for future engineering applications.

3.7. Microstructure Analysis

As mentioned previously, the rapid heating and cooling cycle created by most forms of additive manufacturing processes results in a heavily martensitic microstructure. In the case of Ti-6Al-4V, this is characterized by a so called "basket-weave" pattern. The comparison between the microstructure of conventionally wrought Ti-6Al-4V, shown in Figure 15a, and the microstructure of additively manufactured Ti-6Al-4V, shown in Figure 15b, is quite striking. The basket-weave pattern of the

overlapping α' phase is quite visible, compared to the more randomly orientated microstructure produced by more conventional means.

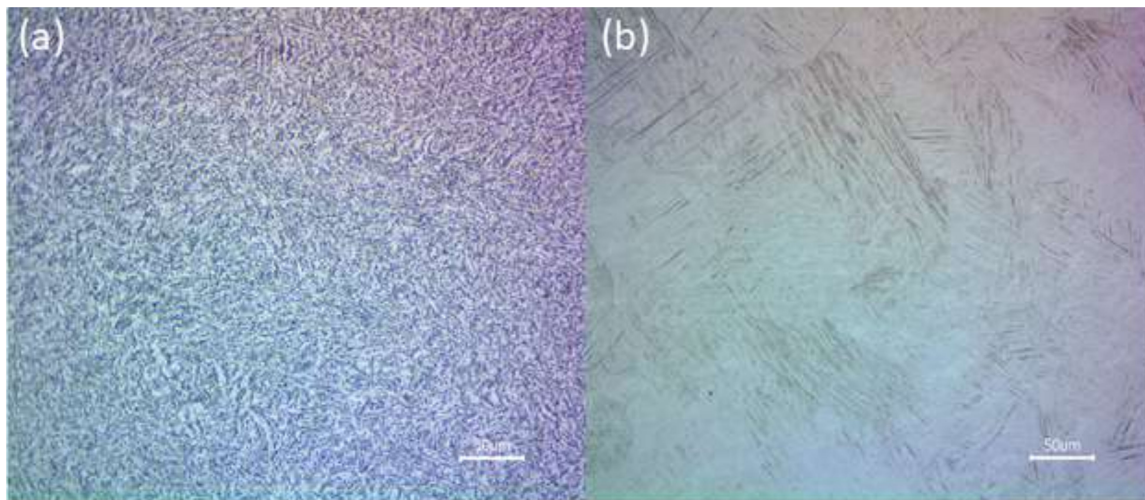


Figure 15. Optical micrographs of (a) Wrought Ti-6Al-4V and (b) DMLS Ti-6Al-4V.

Neither optical microscopy nor electron microscopy of the treated vs. untreated samples showed a significant change in microstructure. In both cases, the distribution of the α' and β phases appear randomly distributed, with no obvious relationship between the β phase and the surface of the specimens, as seen in Figure 16a,b. Due to the low temperatures observed during the cold working (the samples were too hot to touch immediately after processing, but did not show any evidence of oxidization) the samples never reached a point where dynamic recrystallization could occur, so microstructural changes would be unlikely.

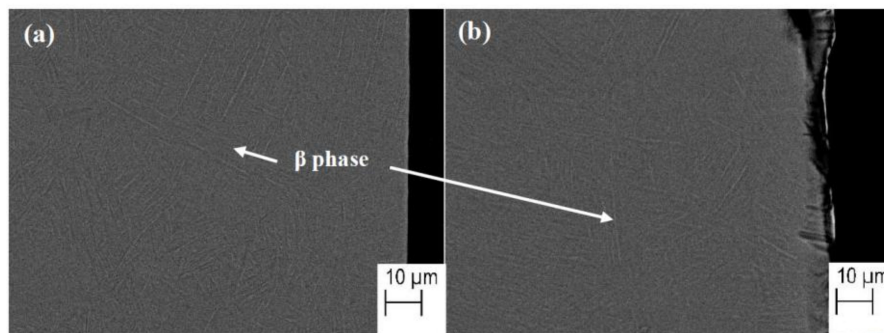


Figure 16. SEM micrographs of (a) UIT applied and (b) untreated specimens, BSE at 30 kV.

In both cases β phase “needles” were observed at various angles to the surface of the sample, and their lengths were relatively consistent with an average 17.2 μm at the surface in the untreated region and an average 16.8 μm at the surface of the treated region, a 2.3% difference. This suggests that the predominant mechanisms of fatigue life improvement are the addition of compressive residual stress and surface roughness improvements.

4. Conclusions

By applying UIT to the surface of DMLS Ti-6Al-4V, a nearly three-fold increase in fatigue life for cyclic stress levels of 400 MPa was achieved. This improvement can be attributed to the several aspects of the treatment, reduction in surface porosity, a decrease in surface roughness and possibly causing local increases in hardness. By cold working the surface, the barrier for crack nucleation is increased and delaying the onset of fatigue cracking at the surface. The large compressive stresses

imposed by UIT on the treated area also suppress crack propagation by offsetting tensile stresses at the surface during cyclic loads. In addition, improved surface finish due to UIT can help to reduce the number of potential sites for crack nucleation by reducing surface porosity, again delaying the onset of crack formation. The impact force of the treatment was determined to be 72 kN and a curve of impact force versus compressive static force was developed. Microstructural observations did not demonstrate any significant change between treated and untreated specimen edges, suggesting the predominant mechanisms of the treatment are the surface modifications and compressive residual stress. In conclusion, UIT can successfully improve the surface finish while simultaneously improve the fatigue life.

Author Contributions: Conceptualization, M.S.A.E., and L.K.; methodology, P.W., S.M., E.T. and S.N.; software, E.T.; validation, E.T., P.W.; formal analysis, E.T. and P.W.; investigation, P.W., S.M., E.T. and S.N.; resources, M.S.A.E.; data curation, E.T., P.W.; writing—original draft preparation, E.T., P.W. and S.N.; writing—review and editing, P.W. and M.S.A.E.; visualization, E.T., P.W. and S.N.; supervision, M.S.A.E.; project administration, M.S.A.E.; funding acquisition, M.S.A.E.

Funding: This research was funded by BOMBARDIER Aerospace of Montreal, in collaboration with CARIC National Forum (grant number CARIC-CRIAQ MDO-1601_TRL4+) and MITACS Canada (grant number IT07461).

Acknowledgments: Mostafa S.A. ElSayed acknowledges the financial support provided by BOMBARDIER Aerospace of Montreal, in collaboration with CARIC National Forum (grant number CARIC-CRIAQ MDO-1601_TRL4+) and MITACS Canada (grant number IT07461). The authors would like to extend their acknowledgements to the employees of the machine shop, and Dix of the X-ray Diffractometry Lab, both at Carleton University for their guidance and patience, the Centre of Photonics Research and Jeff Ovens at the X-ray Core Facility, both at the University of Ottawa for their training and assistance.

Conflicts of Interest: The authors declare no conflict of interest.

References

1. Javid, M.; Haleem, A. Additive manufacturing applications in medical cases: A literature based review. *Alex. J. Med.* **2017**, *54*, 411–422. [[CrossRef](#)]
2. Schiller, G.J. Additive manufacturing for Aerospace. In Proceedings of the 2015 IEEE Aerospace Conference, Big Sky, MT, USA, 7–14 March 2015.
3. Frazier, W.E. Metal Additive Manufacturing: A Review. *J. Mater. Eng. Perform.* **2014**, *23*, 1917–1928. [[CrossRef](#)]
4. Kruth, J.-P.; Leu, M.C.; Nakagawa, T. Progress in Additive Manufacturing and Rapid Prototyping. *CIRP Ann.* **1998**, *47*, 525–540. [[CrossRef](#)]
5. United States Air Force Global Horizons Final Report: United States Air Force Global Science and Technology Vision. 2013. Available online: <https://www.hSDL.org/?abstract&did=741377> (accessed on 8 November 2019).
6. Gebhardt, A.; Jan-Steffen, H.T. *Additive Manufacturing*; Carl Hanser Verlag GmbH & Co. KG: München, Germany, 2016.
7. Murr, L.E.; Gaytan, S.M.; Ceylan, A.; Martinez, E.; Martinez, J.L.; Hernandez, D.H.; Machado, B.I.; Ramirez, D.A.; Medina, F.; Collins, S.; et al. Characterization of titanium aluminide alloy components fabricated by additive manufacturing using electron beam melting. *Acta Mater.* **2010**, *58*, 1887–1894. [[CrossRef](#)]
8. Kruth, J.-P.; Mercelis, P.; Vaerenbergh, V.J.; Froyen, L.; Rombouts, M. Binding mechanisms in selective laser sintering and selective laser melting. *Rapid. Prototyp. J.* **2005**, *1*, 26–36. [[CrossRef](#)]
9. Gorny, B.; Niendorf, T.; Lackmann, J.; Thoene, M.; Troester, T.; Maier, H. In Situ Characterization of the Deformation and Failure Behavior of Non-Stochastic Porous Structures Processed by Selective Laser Melting. *Mater. Sci. Eng. A* **2011**, *27*, 2–7.
10. Ciocca, L.; Fantini, M.; de Crescenzo, F.; Corinaldesi, G.; Scoti, R. Direct metal laser sintering (DMLS) of a customized titanium mesh for prosthetically guided bone regeneration of atrophic maxillary arches. *Med. Biol. Eng. Comput.* **2011**, *49*, 1347–1352. [[CrossRef](#)] [[PubMed](#)]
11. Ning, F.; Cong, W.; Qiu, J.; Wei, J.; Wang, S. Additive manufacturing of carbon fiber reinforced thermoplastic composites using fused deposition modeling. *Compos. Part B Eng.* **2015**, *80*, 369–378. [[CrossRef](#)]

12. Herzog, D.; Seyda, V.; Wycisk, E.; Emmelmann, C. Additive manufacturing of metals. *Acta Mater.* **2016**, *117*, 371–392. [[CrossRef](#)]
13. Milewski, J.O. *Additive Manufacturing of Metals: From Fundamental Technology to Rocket Nozzles, Medical Implants, and Custom Jewelry*; Springer International Publishing AG: Cham, Switzerland, 2017.
14. Mueller, B. Additive Manufacturing Technologies—Rapid Prototyping to Direct Digital Manufacturing. *Assem. Autom.* **2012**, *32*. [[CrossRef](#)]
15. Deckers, J.; Vleugels, J.; Kruth, J.-P. Additive Manufacturing of Ceramics: A Review. *J. Ceram. Sci. Technol.* **2014**, *5*, 245–260.
16. Bos, F.; Wolfs, R.; Ahmed, Z.; Salet, T. Additive manufacturing of concrete in construction: Potentials and challenges of 3D concrete printing. *Virtual Phys. Prototype* **2016**, *11*, 209–225. [[CrossRef](#)]
17. Stansbury, J.W.; Idacavage, M.J. 3D printing with polymers: Challenges among expanding options and opportunities. *Dent. Mater.* **2016**, *32*, 54–64. [[CrossRef](#)] [[PubMed](#)]
18. Guo, N.; Leu, M.C. Additive manufacturing: Technology, applications and research needs. *Front. Mech. Eng.* **2013**, *8*, 215–243. [[CrossRef](#)]
19. Spierings, A.B.; Starr, T.L.; Wegener, K. Fatigue performance of additive manufactured metallic parts. *Rapid Prototype J.* **2013**, *19*, 88–94. [[CrossRef](#)]
20. Islam, M.; Purtonen, T.; Piili, H.; Salminen, A.; Nyrhila, O. Temperature Profile and Imaging Analysis of Laser Additive Manufacturing of Stainless Steel. *Phys. Procedia* **2013**, *41*, 835–842. [[CrossRef](#)]
21. Kanagarajah, P.; Brenne, F.; Niendorf, T.; Maier, H.J. Inconel 939 processed by selective laser melting: Effect of microstructure and temperature on the mechanical properties under static and cyclic loading. *Mater. Sci. Eng. A* **2013**, *588*, 188–195. [[CrossRef](#)]
22. Vilaro, T.; Colin, C.; Bartout, J.D.; Naze, L.; Sennour, M. Microstructural and mechanical approaches of the selective laser melting process applied to a nickel-base superalloy. *Mater. Sci. Eng. A* **2012**, *534*, 446–451. [[CrossRef](#)]
23. Schimidtke, K.; Palm, F.; Hawkins, A.; Emmelmann, C. Process and Mechanical Properties: Applicability of a Scandium modified Al-alloy for Laser Additive Manufacturing. *Phys. Procedia* **2011**, *12*, 369–374. [[CrossRef](#)]
24. Brandl, E.; Heckenberger, U.; Holzinger, V.; Buchbinder, D. Additive manufactured AlSi10Mg samples using Selective Laser Melting (SLM): Microstructure, high cycle fatigue, and fracture behavior. *Mater. Des.* **2012**, *34*, 159–169. [[CrossRef](#)]
25. Hrabe, N.W.; Quinn, T.P.; Kircher, R. Effects of Processing on Microstructure and Mechanical Properties of Ti-6Al-4V Fabricated using Electron Beam Melting (EBM), Part 1: Distance from Build Plate and Part Size. *Mater. Sci. Eng. A* **2013**, *573*, 264–270. [[CrossRef](#)]
26. Chan, K.S.; Koike, M.; Mason, R.L.; Okabe, T. Fatigue Life of Titanium Alloys Fabricated by Additive Layer Manufacturing Techniques for Dental Implants. *Metall. Mater. Trans. A* **2013**, *44*, 1010–1022. [[CrossRef](#)]
27. Conner, B.P.; Manogharan, G.P.; Martof, A.N.; Rodomsky, L.M.; Rodomsky, C.M.; Jordan, D.C.; Limperos, J.W. Making sense of 3-D printing: Creating a map of additive manufacturing products and services. *Addit. Manuf.* **2014**, *1*, 64–76. [[CrossRef](#)]
28. Marcus, H.; Barlow, J.; Beaman, J.; Bourell, D.; Agarwala, M. Direct selective laser sintering of metals. *Rapid Prototype J.* **1995**, *1*, 26–36.
29. Sames, W.J.; List, F.A.; Pannala, S.; Dehoff, R.R.; Babu, S.S. The metallurgy and processing science of metal additive manufacturing. *Int. Mater. Rev.* **2016**, *61*, 315–360. [[CrossRef](#)]
30. Metal AM. Applications for metal Additive Manufacturing Technology. Available online: <https://www.metal-am.com/introduction-to-metal-additive-manufacturing-and-3d-printing/applications-for-additive-manufacturing-technology/> (accessed on 8 November 2019).
31. Vayre, B.; Vignat, F.; Villeneuve, F. Designing for Additive Manufacturing. *Procedia CIRP* **2012**, *3*, 632–637. [[CrossRef](#)]
32. Leuders, S.; Thone, M.; Riemer, A.; Niendorf, T.; Troster, T.; Richard, H.A.; Maier, H.J. On the mechanical behaviour of titanium alloy TiAl6V4 manufactured by selective laser melting: Fatigue resistance and crack growth performance. *Int. J. Fatigue* **2013**, *48*, 300–307. [[CrossRef](#)]
33. Santos, E.C.; Abe, F.; Osakada, K.; Kitamura, Y.; Shiomo, M. Mechanical properties of pure titanium models processed by selective laser melting. In Proceedings of the Solid Freeform Fabrication Symposium, Austin, TX, USA, 5–7 August 2002; pp. 180–186.

34. Li, P.; Warner, D.H.; Fatemi, A.; Phan, N. Critical assessment of the fatigue performance of additively manufactured Ti-6Al-4V and perspective for future research. *Int. J. Fatigue* **2016**, *85*, 130–143. [CrossRef]
35. Ashan, M. 3D Printing and Titanium Alloys: A Paper Review. *Eur. Acad. Res.* **2016**, *3*.
36. Tomlin, M.; Meyer, J. Topology Optimization of an Additive Layer Manufactured (ALM) Aerospace Part. In Proceedings of the 7th Altair CAE Technology Conference 2011, Warwickshire, UK, 10 May 2011.
37. Edwards, P.; Ramulu, M. Fatigue performance evaluation of selective laser melted Ti-6Al-4V. *Mater. Sci. Eng. A* **2014**, *598*, 327–337. [CrossRef]
38. Wycisk, E.; Solbach, A.; Siddique, S.; Herzog, D.; Walther, F.; Emmelmann, C. Effects of Defects in Laser Additive Manufactured Ti-6Al-4V on Fatigue Properties. *Phys. Procedia* **2014**, *56*, 371–378. [CrossRef]
39. Li, S.J.; Murr, L.E.; Cheng, X.Y.; Zhang, Z.B.; Hao, Y.L.; Yang, R.; Medina, F.; Wicker, R.B. Compression fatigue behavior of Ti-6Al-4V mesh arrays fabricated by electron beam melting. *Acta Mater.* **2012**, *60*, 793–802. [CrossRef]
40. Mercelis, P.; Kruth, J.-P. Residual stresses in selective laser sintering and selective laser melting. *Rapid Prototype J.* **2006**, *12*, 254–265. [CrossRef]
41. Sher, D. GE Aviation Already 3D Printed 30,000 Fuel Nozzles for its LEAP Engine. 3D Printing Media Network. Available online: <https://www.3dprintingmedia.network/ge-aviation-already-3d-printed-30000-fuel-nozzles-for-its-leap-engine/> (accessed on 19 May 2019).
42. Zhan, K.; Jiang, C.H.; Ji, V. Residual Stress Relaxation of Shot Peened Deformation Surface Layer on S30432 Austenite Steel under Applied Loading. *Mater. Trans.* **2012**, *53*, 1578–1581. [CrossRef]
43. Ma, C.; Andani, M.T.; Qin, H.; Moghaddam, N.S.; Ibrahim, H.; Jahadakbar, A.; Amerinatanzi, A.; Ren, Z.; Zhang, H.; Doll, G.L.; et al. Improving surface finish and wear resistance of additive manufactured nickel-titanium by ultrasonic nano-crystal surface modification. *J. Mater. Process. Technol.* **2017**, *249*, 433–440. [CrossRef]
44. Ma, C.; Dong, Y.; Ye, C. Improving Surface Finish of 3D-printed Metals by Ultrasonic Nanocrystal Surface Modification. *Procedia CIRP* **2016**, *45*, 319–322. [CrossRef]
45. Wang, Y.; Sheng, A. *Manufacturing and Engineering Technology*; CRC Press: Boca Raton, FL, USA, 2014; p. 1.
46. Ye, C.; Telang, A.; Gill, A.; Wen, X.; Mannava, S.R.; Qian, D.; Vasudevan, V.K. Effects of Ultrasonic Nanocrystal Surface Modification on the Residual Stress, Microstructure, and Corrosion Resistance of 304 Stainless Steel Welds. *Metall. Mater. Trans. A* **2018**, *49*, 972–978. [CrossRef]
47. Cattoni, D.; Ferrari, C.; Lebedev, L.; Pazos, L.; Svoboda, H. Effect of Blasting on the Fatigue Life of Ti-6Al-7Nb and Stainless Steel AISI 316 LVM. *Procedia Mater. Sci.* **2012**, *1*, 461–468. [CrossRef]
48. Statnikov, E.S.; Korolkov, O.V.; Vityazev, V.N. Physics and Mechanism of Ultrasonic Impact. *Ultrasonics* **2006**, *44*, e533–e538. [CrossRef]
49. Statnikov, E.S.; Muktepavel, V.O.; Blomqvist, A. Comparison of Ultrasonic Impact Treatment (UIT) and Other Fatigue Life Improvement Methods. *Weld. World* **2002**, *46*, 20–32. [CrossRef]
50. Mordyuk, B.N.; Prokopenko, G.I. Ultrasonic impact peening for the surface properties' management. *J. Sound Vib.* **2007**, *308*, 855–866. [CrossRef]
51. Dekhtyar, A.I.; Mordyuk, B.N.; Savvakina, D.G.; Bondarchuk, V.I.; Moiseeva, I.V.; Khripta, N.I. Enhanced fatigue behavior of powder metallurgy Ti-6Al-4V alloy by applying ultrasonic impact treatment. *Mater. Sci. Eng. A* **2015**, *641*, 348–359. [CrossRef]
52. Ikeda, S.; Kobayashi, Y.; Matsui, A. Evaluation of shot peening impact force by AE method. In Proceedings of the 12th International Conference on Shot Peening, Goslar, Germany, 15–18 September 2014; pp. 244–249.
53. DeClark, B.W.; Loersch, J.F.; Neal, J.W.; Weber, J.H. Shot Peening Intensity Detector. U.S. Patent 4,470,292, 11 September 1984.
54. Statnikov, E.S.; Vityazev, V.N.; Korolkov, O.V. Study of comparative characteristics of ultrasonic impact and optimization of deformation treatment processes. In Proceedings of the 5th World Congress on Ultrasonics, Paris, France, 5–7 September 2003.
55. ASTM International. *Standard Practice for Conducting Force Controlled Constant Amplitude Axial Fatigue Tests of Metallic Materials*; ASTM E466-15; ASTM International: West Conshohocken, PA, USA, 2015.
56. OmniSint-160. 2015. Available online: http://lasersint.com/wordpress/?page_id=449 (accessed on 12 September 2019).
57. GE Additive, Ti-6Al-4V Grade 23. 2019. Available online: <https://www.ge.com/additive/additive-manufacturing/materials/apc/ti-6al-4v-23> (accessed on 27 August 2019).

58. EOS, EOS M290/400W Standard, AD, WEIL. 2014. Available online: <https://www.sculpteo.com/media/imagecontent/EOS-Titanium-Ti64ELI.pdf> (accessed on 28 August 2019).
59. Qiu, C.; Adkins, N.J.E.; Attallah, M.M. Microstructure and tensile properties of selectively laser-melted and of HIPed laser-melted Ti-6Al-4V. *Mater. Sci. Eng. A* **2013**, *578*, 230–239. [CrossRef]
60. Dimla, D.E.; Hopkinson, N.; Rothe, H. Investigation of complex rapid EDM electrodes for rapid tooling applications. *Int. J. Adv. Manuf. Technol.* **2004**, *23*, 249–255. [CrossRef]
61. Emery Cloth Sheet 220–240 Grit. 2019. Available online: <https://www.stuller.com/products/10-11014/56351/?groupId=190773> (accessed on 27 August 2019).
62. Ultrasonics, D. 20k1200w Ultrasonic Portable Spot Welding Machine. 2019. Available online: <http://www.dowellsonic.com/product/20k1200w-ultrasonic-portable-spot-welding-machine.html> (accessed on 28 August 2019).
63. CNC Parts Department. Fagor 8035 CNC. Available online: <https://www.cncpd.com/product-category/cnc-controllers/fagor-automation/fagor-8035/> (accessed on 28 August 2019).
64. Günther, J.; Krewerth, D.; Lippmann, T.; Leuders, S.; Tröster, T.; Weidner, A.; Biermann, H.; Niendorf, T. Fatigue life of additively manufactured Ti-6Al-4V in the very high cycle fatigue regime. *Int. J. Fatigue* **2017**, *94*, 236–245. [CrossRef]
65. Zhang, H.; Chiang, R.; Qin, H.; Ren, Z.; Hou, X.; Lin, D.; Doll, G.L.; Vasudevan, V.K.; Dong, Y.; Ye, C. The effects of ultrasonic nanocrystal surface modification on the fatigue performance of 3D-printed Ti64. *Int. J. Fatigue* **2017**, *103*, 136–146. [CrossRef]
66. Mc Master-Carr. Compression Springs. 2019. Available online: <https://www.mcmaster.com/springs> (accessed on 17 August 2019).
67. CIMSTAR@QUAL STAR C Product Information Flyer. 2011. Available online: <http://www.cimcool.com/wp-content/uploads/manage-msdspif/pif/CIMSTAR%20QUALSTAR%20C.pdf> (accessed on 21 Aug 2019).
68. MTS, MTS 810 & 858 Test Systems. 2006. Available online: https://www.upc.edu/sct/documents_equipament/d_77_id-412.pdf (accessed on 21 July 2019).
69. AmScope, 18MP USB 3.0 Color CMOS C-Mount Microscope Camera with Reduction Lens. 2019. Available online: <https://www.amscope.com/cameras/18mp-usb3-0-real-time-live-video-microscope-digital-camera.html> (accessed on 19 July 2019).
70. Zeiss, ZEISS GeminiSEM. 2019. Available online: <https://www.zeiss.com/microscopy/int/products/scanning-electron-microscopes/geminisem.html> (accessed on 18 August 2019).
71. Bruker, The Gold Standard in Stylus Profilometry. 2019. Available online: <https://www.bruker.com/products/surface-and-dimensional-analysis/stylus-profilometers/dektak-xt/overview.html> (accessed on 15 August 2019).
72. ASTM International. *Standard Test Methods for Rockwell Hardness of Metallic Materials*; ASTM E18-18a; ASTM International: West Conshocken, PA, USA, 2018.
73. Bowers Group. Portable Hardness Tester IPX-360. Available online: <https://www.bowersgroup.co.uk/ca/product-range/testing-instruments/portable/ipx-360-portable-hardness-tester-ipx-360.html> (accessed on 18 August 2019).
74. Flitzpatrick, M.E.; Fry, A.T.; Holdway, P.; Kandil, F.A.; Shackleton, J.; Suominen, L. Determination of Residual Stresses by X-ray Diffraction. In *Measurement Good Practice Guide No. 52*; National Physical Laboratory: Teddington, UK, 2005; Volume 52, Issue 2, pp. 1–68.
75. Ruud, C.O. A Review of Nondestructive Methods for Residual Stress Measurement. *JOM* **1981**, *33*, 35–40. [CrossRef]
76. Schajer, G.S.; Ruud, C.O. *Practical Residual Stress Measurement Methods*; John Wiley & Sons Ltd.: Hoboken, NJ, USA, 2013.
77. Malvern Panalytical. Empyrean. 2019. Available online: <https://www.malvernpanalytical.com/en/products/product-range/empyrean-range/empyrean> (accessed on 21 August 2019).
78. Zyl, I.V.; Yadroitsava, I.; Yadroitsev, I. Residual stress in ti6al4v objects produced by direct metal laser sintering. *S. Afr. J. Ind. Eng.* **2016**, *27*, 134–141.
79. Novovic, D.; Dewes, R.C.; Aspinwall, D.K.; Voice, W.; Bowen, P. The effect of machined topography and integrity on fatigue life. *Int. J. Mach. Tools Manuf.* **2004**, *44*, 125–134. [CrossRef]
80. Teledyne LeCroy. WaveSurfer 3000 Oscilloscopes. 2019. Available online: <https://teledynelecroy.com/options/productseries.aspx?mseries=466&groupid=234> (accessed on 28 August 2019).

81. ANAMET, Mounting Polymers. 2016. Available online: http://www.anamet.com/media/other/357089-CATALOG_6_mounting_EN.pdf (accessed on 11 July 2019).
82. Allied High Tech Products. Metprep 3™ Grinder/Polisher with Power Head. 2019. Available online: <http://www.alliedhightech.com/Equipment/metprep-3-grinder-polisher-with-powerhead> (accessed on 11 August 2019).
83. Sigma-Aldrich, Aluminum Oxide. 2019. Available online: <https://www.sigmaaldrich.com/catalog/product/sigald/229423?lang=en®ion=CA> (accessed on 8 August 2019).
84. American Society for Testing and Materials. *Standard Practice for Microetching Metals and Alloys*; E 407–99; American Society for Testing and Materials: West Conshohocken, PA, USA, 1999.
85. Deutsches Institut Fur Normung. *DIN 50100: Load Controlled Fatigue Testing—Execution and Evaluation of Cyclic Tests at Constant Load Amplitudes on Metallic Specimens and Components*; Deutsches Institut Fur Normung: Berlin, Germany, 2016.
86. Alang, N.A.; Razak, N.A.; Miskam, A.K. Effect of Surface Roughness on Fatigue Life of Notched Carbon Steel. *Int. J. Eng. Technol.* **2011**, *11*, 160–163.



© 2019 by the authors. Licensee MDPI, Basel, Switzerland. This article is an open access article distributed under the terms and conditions of the Creative Commons Attribution (CC BY) license (<http://creativecommons.org/licenses/by/4.0/>).